4-2023

Chlorophyll Dynamics from Sentinel-3 Using an Optimized Algorithm for Enhanced Ecological Monitoring in Complex Urban Estuarine Waters

Jonathan Sherman
CUNY City College

Maria Tzortziou
CUNY City College

Kyle J. Turner
CUNY City College

Joaquim Goes
Columbia University

Brice Grunert
Cleveland State University

International Journal of Applied Earth Observation and Geoinformation 118 (2023) 103223

Contents lists available at ScienceDirect

International Journal of Applied Earth Observations and Geoinformation

journal homepage: www.elsevier.com/locate/jag

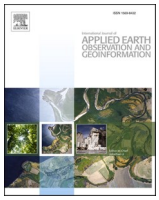

Chlorophyll dynamics from Sentinel-3 using an optimized algorithm for enhanced ecological monitoring in complex urban estuarine waters

Jonathan Sherman [a], Maria Tzortziou [a,*], Kyle J. Turner [a], Joaquim Goes [b], Brice Grunert [c]

[a] Department of Earth and Atmospheric Sciences, The City College of New York, The City University of New York, 160 Convent Avenue, New York, NY 10031, USA
[b] Marine Biology, Department of Marine Biology and Paleoenvironment, Lamont–Doherty Earth Observatory, Columbia University, 61 Route 9W, Palisades, NY 10964, USA
[c] Biological, Geological, and Environmental Sciences, Cleveland State University, 2121 Euclid Avenue, Cleveland, OH 44115, USA

ARTICLE INFO

Keywords:
Chlorophyll-*a*
Ocean color
Estuaries
Water quality
Long Island Sound

ABSTRACT

Urban estuaries are dynamic environments that hold high ecological and economic value. Yet, their optical complexity hinders accurate satellite retrievals of important biogeochemical variables, such as chlorophyll-*a* (Chl-*a*) biomass. Approaches based on a limited number of satellite spectral bands often fail to capture seasonal transitions and sharp spatial gradients in estuarine Chl-*a* concentrations, inhibiting integration of satellite data into water quality monitoring and conservation programs. We propose a novel approach that utilizes the wide range of spectral information captured by the Ocean and Land Color Instrument (OLCI) to retrieve estuarine Chl-*a*. To validate our approach, we used measurements in Long Island Sound (LIS), a highly urbanized estuary increasingly susceptible to anthropogenic stressors and climate change. Hyperspectral remote sensing reflectance (R_{rs}) and Chl-*a* data representing the spatiotemporal diversity of LIS were used to assess the ideal atmospheric correction approach for OLCI and develop a multi-spectral multiple linear regression (MS-MLR) Chl-*a* algorithm. POLYMER derived R_{rs} proved to be the preferred atmospheric correction approach. Evaluation of MS-MLR performance in retrieving Chl-*a* with *in situ* R_{rs} showed good agreement with field measurements. Application to OLCI-retrieved R_{rs} showed significant improvement (20%-30%) in common error metrics relative to other algorithms assessed. The MS-MLR approach successfully captured seasonal cycles and spatial gradients in Chl-*a* concentration. Application of this method to urban estuaries and coasts enables accurate, high resolution Chl-*a* observations at the ecosystem scale and across a range of conditions, as needed for conservation and ecosystem management efforts.

1. Introduction

Estuaries and coastal oceans are dynamic environments that play a critical role in the global carbon cycle (Bauer et al., 2013) and provide many ecosystem services (Boerema and Meire, 2017). In these regions, biogeochemical processes are intrinsically linked to large fluxes of dissolved and particulate matter from land and are subject to increasing anthropogenic and climate pressures. Combined, these processes impact estuarine and coastal water quality. One important indicator of water quality and ecosystem health is chlorophyll-*a* (Chl-*a*) concentration, routinely used as a proxy for phytoplankton biomass and an indicator of a system's trophic state (Boyer et al., 2009). Phytoplankton are critical to aquatic systems, however, excessive phytoplankton blooms can lead to deteriorated water quality (e.g., eutrophication, hypoxia) (Boyer et al., 2009; Livingston, 2007). As such, consistent, frequent, and accurate monitoring of Chl-*a* is essential for the effective management and protection of nearshore ecosystems, especially along urbanized coastlines.

In many urban estuaries, programs have been established to monitor water quality at fixed stations sampled periodically (Haraguchi et al., 2015; Staehr et al., 2017). These programs are valuable to understand how natural and anthropogenic stressors impact water quality. Yet, they can only cover a fraction of the spatiotemporal scales of estuarine biogeochemical variability and are further limited by inclement weather or, as relevant to 2020, restrictions caused by the COVID-19 pandemic. Moreover, assessing the spatiotemporal extent of blooms and their connections to other processes based on monthly or biweekly point measurements is challenging. To complement *in situ* sampling, satellite

* Corresponding author.
E-mail address: mtzortziou@ccny.cuny.edu (M. Tzortziou).

https://doi.org/10.1016/j.jag.2023.103223
Received 5 October 2022; Received in revised form 28 December 2022; Accepted 3 February 2023
Available online 28 February 2023

ocean color observations provide a unique and valuable tool for monitoring Chl-*a* dynamics across a range of spatiotemporal scales.

Ocean color Chl-*a* algorithms are based on two main approaches, empirical and semi-analytical models. Empirical models are based on statistical relationships between Chl-*a* concentrations and remote sensing reflectance (R_{rs}), from simple band-ratio approaches to more complex machine learning (ML) neural network algorithms (Hu et al., 2012; O'Reilly et al., 1998; O'Reilly and Werdell, 2019; Pahlevan et al., 2020). Semi-analytical models relate R_{rs} to the inherent optical properties (IOPs) of the water comprised of absorption by phytoplankton, colored dissolved organic matter (CDOM) or non-algal particles and scattering by particles, and then derive Chl-*a* from empirical relationships between *in situ* phytoplankton absorption and Chl-*a* concentrations (O'Reilly et al., 1998). Common semi-analytical models include the Garver–Siegel–Maritorena Model (Maritorena et al., 2002) and the Generalized Inherent Optical Property model (Werdell et al., 2013). Algorithms for global scale Chl-*a* retrievals based on blue-green wavelengths work remarkably well for open ocean waters where phytoplankton absorption dominates the IOPs (Werdell et al., 2018), yet perform poorly in optically complex coastal systems, either overestimating Chl-*a* concentrations and blooms or missing them altogether (Freitas and Dierssen, 2019). Several studies in complex turbid waters have recommended retrievals that rely on the red portion of the spectrum where CDOM and non-algal particle absorption are negligible. These include algorithms based on red-band differences (RBD) (Freitas and Dierssen, 2019; Gitelson, 1992), red and near-infrared (NIR) ratios (Gilerson et al., 2010; Moses et al., 2012), green-to-red band ratios (Le et al., 2013), and red and NIR chlorophyll fluorescence line height (Hu et al., 2005). These algorithms have shown improvements over global blue/green band ratio models, however at lower Chl-*a* concentrations red bands become less sensitive to Chl-*a* impeding their use alone (Pahlevan et al., 2020). Moreover, varying contributions by particulate backscattering in the red part of the spectrum and transitions in phytoplankton community structure present additional challenges in turbid estuaries.

To avoid the limitations of relying on either the blue or red bands alone, here, we present a new empirical Chl-*a* algorithm that, rather, utilizes R_{rs} information across a wide (blue to red) spectral range and is optimized for optically complex waters based on a Multi-Spectral, Multiple Linear Regression (MS-MLR) between R_{rs} and Chl-*a* for Sentinel-3A/B (OLCI). MLR algorithms have been previously used to successfully retrieve CDOM and DOC concentrations in optically complex systems (Cao et al., 2018; Cao and Tzortziou, 2021; Mannino et al., 2014). An MLR approach is advantageous as it relies on the absolute magnitude of R_{rs} at multiple spectral bands as well as accounts for the spectral shape of R_{rs}. Both are critical for differentiating between Chl-*a* and CDOM and other water constituents that impact the degree of optical complexity in urban estuaries. The OLCI instrument on board the Sentinel-3A/B (S3A, S3B) satellites is part of the European Space Agency Earth observation initiative and has provided ocean color data since May 2016. OLCI provides R_{rs} at 21 spectral bands (11 of which are between 400 nm and 709 nm) with a ground resolution of 300 m. The combination of S3A and S3B result in near-daily coverage. The high spatiotemporal resolutions make OLCI an excellent choice for application of an optimized, multi-spectral Chl-*a* algorithm for highly variable nearshore environments.

For this study, the Long Island Sound estuary (LIS) was chosen to test the MS-MLR development and application. The MS-MLR algorithm was developed using coincident *in situ* Chl-*a* concentration and hyperspectral R_{rs} measurements collected across LIS. Before developing the MS-MLR, we assessed several atmospheric correction (AC) algorithms for their ability to accurately retrieve R_{rs} from OLCI in LIS. This is critical as urban emissions and pollution result in highly dynamic atmospheric aerosol composition and trace gas concentrations, which, if unaccounted for, introduce large errors to estimated R_{rs} (Tzortziou et al., 2018).

LIS is a large estuary (3420 km^2) on the northeast U.S. coast that is densely populated and highly developed, particularly in its western region. LIS and its watershed basin support diverse ecological ecosystems that provide ecosystem services valued as high as $37 billion per year (Kocian et al., 2015). Despite its ecological and socioeconomic value, LIS suffers from water quality issues, including eutrophication, seasonal hypoxia, and recurrent harmful algal blooms (Anderson and Taylor, 2001; Whitney and Vlahos, 2021). Extensive *in situ* monitoring efforts have been routinely conducted in LIS by local communities and municipal/state departments including the Connecticut Department of Energy and Environmental Protection (CTDEEP), New York City Environmental Protection (NYC-DEP), and Save the Sound. Across LIS, Chl-*a* concentration displays a strong gradient, with high values in the west that decrease towards the east. This gradient is attributed to significantly higher nitrogen loading in the west from the urbanized NYC metro area (Latimer et al., 2014). LIS also displays a relatively consistent seasonal cycle with a spring bloom occurring typically between February and April, followed by a summer bloom that usually peaks in August (Latimer et al., 2014). Understanding the drivers and extent of these Chl-*a* trends is critical, as they drive seasonal hypoxia that poses a major threat to LIS, particularly in the western region where stratification is typically stronger and oceanic exchange is limited (Welsh and Eller, 1991; Whitney and Vlahos, 2021). Historically, summer-time hypoxia in the western Sound has been linked to high levels of Chl-*a* during the preceding spring (CTDEEP, 2018).

In this study we developed an optimized Chl-*a* algorithm for highly complex waters that uses the full range of spectral information measured by OLCI. Hyperspectral R_{rs} and Chl-*a* data representing the spatiotemporal diversity of LIS were used to, first, assess the ideal atmospheric correction approach for OLCI and, then, design and evaluate the performance of the Chl-*a* algorithm. Our results highlight how such an optimized algorithm can greatly contribute to water quality monitoring efforts across a range of conditions, as needed for conservation and ecosystem management efforts in urban coastal systems.

2. Methods

2.1. In situ data collection

To develop the MS-MLR algorithm, concurrent Chl-*a* and hyperspectral R_{rs} were collected throughout LIS between July 2018 and February 2022 (39 surveys), capturing seasonal transitions and a range of environmental conditions (Fig. 1). Data in the LIS mainstem were collected onboard *R/V John Dempsey* in collaboration with the CTDEEP water quality monitoring program that includes monthly to bi-monthly sampling at multiple stations across western-to-eastern LIS (Fig. 1). To extend the spatial coverage, we collected additional data with small boats within and around main river inputs into LIS, the Connecticut and Housatonic Rivers (Fig. 1).

2.1.1. Chl-a measurements

Following Holm-Hansen et al. (1965) water samples were collected in amber HDPE bottles from surface waters (0.5 m) using a Niskin bottle and vacuum filtered through 25 mm Whatman GF/F filters (0.7 μm pore size), flash frozen and stored at −20 °C until further analysis. Chl-*a* was extracted overnight in 90% acetone (4 mL) followed by fluorometric analysis with a Turner Trilogy Fluorometer® before and after acidifying the sample. At each station, Chl-*a* was measured in duplicate and averaged. The mean duplicate difference for the whole dataset was 3.8%. Duplicates with difference > 50% were excluded from the analysis (N = 6).

2.1.2. Hyperspectral remote sensing reflectance

Above-water hyperspectral R_{rs} was measured using a handheld Spectra Vista Corporation HR512-i spectroradiometer (SVC)®. The SVC provides hyperspectral measurements between 350 and 1050 nm at a sampling interval of ≤ 1.5 nm and a 4° field-of-view. Measurements were collected following standard protocols (Zibordi et al., 2019). This

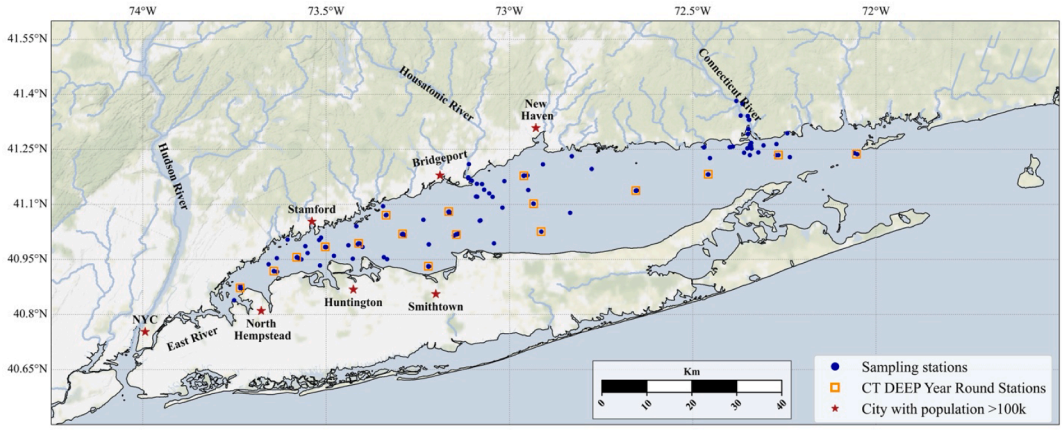

Fig. 1. Long Island Sound. Blue dots represent concurrent Chl-*a* and R_{rs} measurements. Orange squares denote CTDEEP stations sampled year-round.

included sequential scans of a reference plaque (Spectralon), sky, and water surface at a 40° viewing angle and sun-relative azimuth of 90°-135°. For quality control, five successive scans were conducted for each measurement type. Care was taken to avoid perturbations created by the ship's superstructure or floating debris or foam on the water surface. The mean R_{rs} was then calculated from the SVC successive spectra using the three-component (3C) glint model (Groetsch et al., 2017). The 3C model has been shown to more effectively remove residual skylight and sun glint and produce more accurate R_{rs} calculations for above-water spectral measurements in sub-optimal sky conditions compared with the standard approach of Mobley (1999) (Pitarch et al., 2020; Turner et al., 2022). The full workflow for the SVC data processing is available online (https://github.com/tzortziou-lab). For a direct comparison with OLCI-retrieved R_{rs}, *in situ* SVC spectra were weighted to OLCI spectral bands using the spectral response functions of S3A and S3B obtained from NASA's ocean color website (https://oceancolor.gsfc.nasa.gov/docs/rsr/rsr_tables/).

2.2. OLCI data

OLCI S3A and S3B datasets were acquired from NASA's Ocean Biology Processing Group (https://oceancolor.gsfc.nasa.gov/). OLCI data included Level-1B, Full Resolution, Top of Atmosphere radiances that cover the entire LIS region between May 2016-November 2021 (S3B data starts in May 2018). We evaluated three AC approaches for OLCI, (i) NASA's standard SeaDAS algorithm, L2gen (v9.5.1) using the iterative two-band NIR correction (Bailey et al., 2010); (ii) the "dark spectrum fitting" approach in ACOLITE (V20221114.0) (Vanhellemont and Ruddick, 2021); and (iii) POLYMER (v4.14), a spectral matching algorithm with improved handling of sun glint and thin clouds (Steinmetz et al., 2011). The latter two algorithms have been used in similar coastal and turbid regions with improved performance compared to standard AC algorithms. Dimensionless water reflectance output from POLYMER were divided by π to convert to R_{rs}. To assess the performance of each AC approach we compered each R_{rs} band with valid matchups with the *in situ* R_{rs} (see Section 2.4 for full match up criteria).

2.3. MS-MLR model development

The entire development of the MS-MLR was done in Python using common modules, primarily, NumPy, Scikit-learn and Pandas. In total, 156 concurrent Chl-*a* and R_{rs} measurements were collected. The dataset was randomly split into a training dataset (70% of the data, N = 109) used to develop the MS-MLR algorithm and a testing dataset (30%, N = 47) used to independently validate algorithm performance. While the split was random, the randomization seed used to initiate the random number generator was selected to produce datasets with similar spatiotemporal distributions that cover the full range of Chl-*a* values (0.9 to 32 mg m^{-1}) observed in LIS and seasonal cycles historically reported (Fig. 2a-c). In addition, it maintained similar distributions in

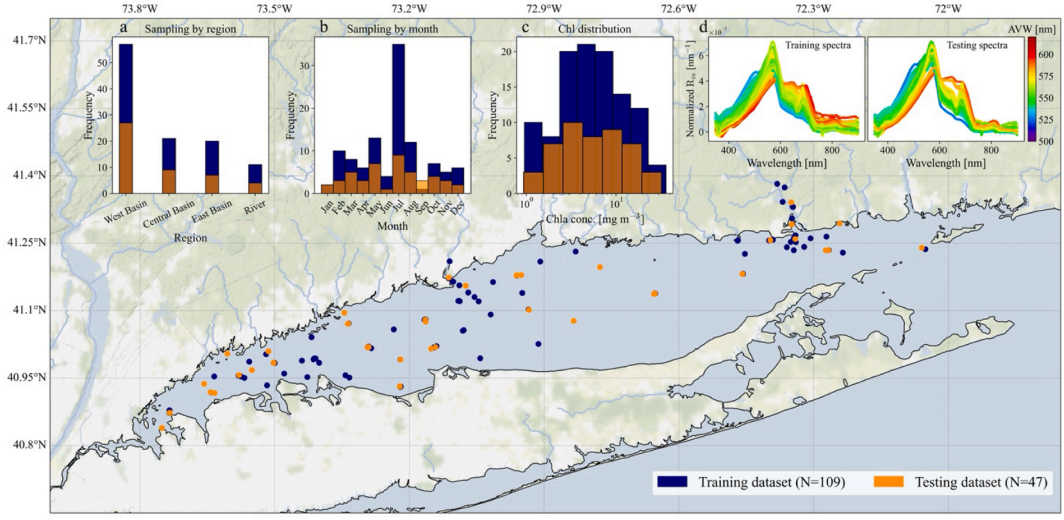

Fig. 2. Spatiotemporal distribution of training (blue) and testing (orange) datasets across LIS. Insets show the distribution of the data by region (a) and month (b). Inset (c) is Chl-*a* concentration distribution. Inset (d) shows the *in situ* R_{rs} spectra for both datasets normalized by their integral and colored by AVW.

Apparent Visible Wavelength (AVW) (Fig. 2d), a spectral classification metric calculated as the weighted harmonic mean of R_{rs} wavelengths (Vandermeulen et al., 2020). In LIS changes in AVW were utilized to effectively capture subtle gradients in phytoplankton, CDOM, and other biogeochemical properties (Turner et al., 2022).

2.3.1. Spectral band selection and MS-MLR model definition

For optimal band selection, we iterated over all possible combinations using five to six bands between 400 and 709 nm. Combination with more bands were excluded to avoid overfitting the model and minimize impacts of multicollinearity between spectral bands. Three criteria were considered: (1) minimizing the Akaike Information Criterion (Cao et al., 2018), (2) including a wide spectral range (blue to red) in R_{rs}, and (3) showing optimal performance when applied to both *in situ* and OLCI data. The MS-MLR algorithm used to estimate Chl-*a* (Chl_{MLR}) was then defined as:

$$Chl_{MLR} = \beta_0 + \beta_1 {}^{*} R_{rs}(443) + \beta_2 {}^{*} R_{rs}(490) + \beta_3 {}^{*} R_{rs}(560) + \beta_4 {}^{*} R_{rs}(674) + \beta_5 {}^{*} R_{rs}(681) \quad (1)$$

Both Chl-*a* and R_{rs} were log-transformed prior to fitting. β_0 is the y-intercept and β_{1-5} are the regression coefficients. To test if collinearity between spectral bands impacts the model output we used both a partial least squares regression, which negates collinearity (Alvarez-Mendoza et al., 2019), and standard ordinary least squares regression. Both methods resulted in identical coefficients.

2.3.2. Determination of MS-MLR model coefficients

Following McKinna et al. (2021), we applied a bootstrapping procedure to the MS-MLR algorithm by subsampling 80% of the training dataset randomly and refitting the model over 1000 iterations. This resulted in a coefficient distribution from which the mean was calculated to determine the final model coefficients. This full developmental process was repeated separately for R_{rs} weighted to S3A and S3B to minimize any difference between the two sensors and their relative spectral response functions. The distribution of each coefficient is provided in Fig. S1. Next, we averaged the two sets of coefficients which can then be applied to spatially and temporally binned OLCI scenes (Table 1).

2.3.3. MS-MLR validation using in situ data

To assess the MS-MLR performance, Chl-*a* was estimated from the *in situ* R_{rs} and compared to the testing dataset. To assess potential interference of non-algal particles and CDOM in the Chl-*a* retrievals, we compared the retrieval to coincident *in situ* measurements of $a_{CDOM}(300)$ (CDOM absorption coefficient at 300 nm), Dissolved Organic Carbon (DOC), and Suspended Particulate Matter (SPM) concentrations.

2.4. Evaluating MS-MLR performance with OLCI satellite data

The final step in the evaluation of the MS-MLR algorithm was to validate Chl_{MLR} retrieved from OLCI S3A/B with field measurements. To increase the number of matchups, Chl-*a* data from CTDEEP were used. For the matchup analysis, we used OLCI scenes within ± 3 h from *in situ* sampling. In each scene, pixels that were not flagged by the bitmask layer as valid or as case2 waters (bitmasks 0 or 1024, respectively) were removed (Steinmetz et al., 2011). For a matchup to be qualified as valid, a 3x3 pixel array centered on a sampling station had to contain at least 5 valid pixels and a coefficient of variation < 0.15 between the pixels for R_{rs} bands 443 nm, 560 nm and 665 nm (Mélin et al., 2011). Accepted matchups were then averaged, resulting in 335 valid matchups.

2.5. Evaluation of additional Chl-a algorithms

Next, we assessed the performance of the MS-MLR in comparison to other global and regional Chl-*a* algorithms commonly used by the ocean color community (See Table S1 for full equations). The first algorithm, Chl_{OC4}, was NASA's standard Chl-*a* algorithm (OC4) using the updated OLCI coefficients (O'Reilly and Werdell, 2019). We also evaluated the RBD algorithm (Chl_{RBD}) (Freitas and Dierssen, 2019). Here, we re-parameterized the coefficients developed for MERIS to OLCI using the same training dataset used to develop the MS-MLR algorithm. Freitas and Dierssen (2019) assigned a background Chl-*a* value when both $R_{rs}(681)$-$R_{rs}(665)$ and $R_{rs}(709)$-$R_{rs}(665)$ were negative, which was the intercept of the $R_{rs}(681)$-$R_{rs}(665)$ fit with Chl-*a* during the summer. We excluded this criterion as it resulted in a constant estimated Chl-*a* value while *in situ* values varied considerably. The third algorithm assessed was the two-band red-NIR ratio algorithm ($Chl_{2\text{-band}}$) (Gilerson et al., 2010; Moses et al., 2012). Lastly, we compared MS-MLR to a machine learning approach, the Mixture Density Network (MDN) algorithm, that also utilizes R_{rs} information across a wide spectral range to derive Chl-*a* (Chl_{MDN}) and has outperformed other algorithms in several nearshore regions and for several operational satellites (Pahlevan et al., 2020). MDN was applied using the publicly available Python package (https://github.com/STREAM-RS).

2.6. Performance metrics

The Mean Absolute Error (MAE) and bias were used to assess each algorithm's accuracy and bias, respectively (Seegers et al., 2018):

$$MAE = 10^{\left(\frac{\sum_{i=1}^{n}\left|\log_{10}\left(x_i^{estimated}\right)-\log_{10}\left(x_i^{measured}\right)\right|}{n}\right)} - 1 \quad (2)$$

$$Bias = 10^{\left(\frac{\sum_{i=1}^{n}\log_{10}\left(x_i^{estimated}\right)-\log_{10}\left(x_i^{measured}\right)}{n}\right)} - 1 \quad (3)$$

To improve and simplify interpretation of these metrics, we subtracted 1 from the MAE and bias (Pahlevan et al., 2022). For example, an MAE of 0.1 represents a 10% relative error in modeled values, while a bias of 0.1 indicates an average overestimation of the algorithm relative to *in situ* of 10%. Conversely a negative bias indicates an average underestimation. For more direct comparison with previous studies, we also calculated the root mean square error (RMSE), root mean square log error (RMSLE), and the median absolute percent error (MAPE), defined as:

$$RMSE = \left(\frac{\sum_{i=1}^{n}\left(x_i^{estimated} - x_i^{measured}\right)^2}{n}\right)^{\frac{1}{2}} \quad (4)$$

$$RMSLE = \left(\frac{\sum_{i=1}^{n}\left(\log_{10}\left(x_i^{estimated}\right) - \log_{10}\left(x_i^{measured}\right)\right)^2}{n}\right)^{\frac{1}{2}} \quad (5)$$

Table 1
MS-MLR coefficients for S3A/B and averaged for OLCI binned scenes. Values in parentheses are the 95% confidence intervals of the coefficient distributions.

	β_0	β_1	β_2	β_3	β_4	β_5
S3A	**0.809** (−0.13, 1.72)	**0.362** (−0.19, 0.91)	**−1.486** (−2.55, −0.41)	**1.879** (1.06, 2.78)	**−9.2** (−10.35, −8.15)	**8.554** (7.44, 9.74)
S3B	**0.713** (−0.3, 1.53)	**0.337** (−0.16, 0.95)	**−1.538** (−2.61, −0.44)	**1.971** (1.16, 2.86)	**−8.917** (−10.01, −7.86)	**8.249** (7.12, 9.4)
MS-MLR	**0.761**	**0.3495**	**−1.512**	**1.925**	**−9.0585**	**8.4015**

$$\text{MAPE} = \text{median}\left(\frac{\left|x_i^{estimated} - x_i^{measured}\right|}{x_i^{measured}}\right) \text{ for } i = 1, \cdots, n \quad (6)$$

In addition, the MS-MLR algorithm was compared with the other algorithms in a pair-wise comparison to calculate the percent win (% win) of each algorithm, i.e., which algorithm is closest to the *in situ* value. The %win was calculated by summing the number of matchups for each algorithm in which their respective residual (=estimated-measured) was lower and then dividing by the total number of matchups to express the value as a percentage (Seegers et al., 2018). Lastly, a Type-II linear regression (reduced major axis) between *in situ* and satellite-retrieved Chl-*a* was used to return the slope and intercept (Freitas and Dierssen, 2019; Trujillo-Ortiz and Hernandez-Walls, 2010).

3. Results and discussion

3.1. Atmospheric correction assessment

A comparison between the R_{rs} values calculated by each AC algorithm and the *in situ* measured R_{rs} showed that POLYMER and L2gen retrieved R_{rs} with significantly lower mean absolute errors ranging from 0.16 to 0.35 (POLYMER) and 0.19 to 0.57 (L2gen) compared to ACOLITE's range of 0.58 to 3.34 (Fig. 3). Similarly, POLYMER and L2gen retrievals were far less biased and had a smaller RMSE. While L2gen performs well in terms of accuracy, it returned far less valid R_{rs} values (31 vs 77 from POLYMER) and POLYMER's error metrics were better (Fig. 3). These results are consistent with similar studies that compared AC algorithms for multi- and hyperspectral satellites in coastal waters (Mograne et al., 2019; Pahlevan et al., 2020). Based on these results, POLYMER was used to derive Level-2 R_{rs}. Fig. S2 provides a full comparison between *in situ* R_{rs} and OLCI R_{rs} derived by POLYMER for all spectral bands from 400 to 709 nm. Fig. S2 indicates that the R_{rs} retrievals at 400, 412 and 709 nm are associated with higher uncertainties, and in the case of 709 nm with a fraction of negative values. As such, these bands were excluded from further use in the MS-MLR algorithm development. This is also consistent with other studies (e.g., Cao et al., 2018).

3.2. MS-MLR performance validation

The performance of the MS-MLR algorithm was first evaluated using OLCI-weighted *in situ* R_{rs} and concurrent Chl-*a* measurements (Fig. 4) that remained independent during development. The MS-MLR algorithm outperformed the algorithms evaluated with the lowest MAE (0.33 compared to values of 0.5–0.98 for the other methods), RMSLE (0.17 vs 0.33–0.39) and MAPE (22% vs 30%-45%). Moreover, MS-MLR displayed minimal bias (0.06), indicating that overall MS-MLR overestimates Chl-*a* by only 6% on average. This greatly contrasts with the high bias of OC4 (0.78). The most significant improvement was observed at lower Chl-*a* concentrations, where OC4 in particular is known to underperform in LIS (Freitas and Dierssen, 2019) (Fig. 4). The intercept and slope of the linear fit between $\text{Chl}_{\text{insitu}}$ and Chl_{MLR} are 0.1 and 0.88, respectively, as opposed to the intercept and slope of 0.43 and 0.73 between $\text{Chl}_{\text{insitu}}$ and Chl_{OC4} (Fig. 4). A similar difference was observed for Chl_{RBD}. $\text{Chl}_{\text{2-band}}$, on the other hand, resulted in a negative intercept and a slope > 1. Chl_{MDN} also performed well with a similar slope and higher intercept, MAPE and MAE to MS-MLR (0.83, 0.19, 30% and 0.5 respectively). In pair-wise comparisons Chl_{MLR} won 72% of the cases. Error propagation was assessed using Monte Carlo simulations (McKinna et al., 2019), where each R_{rs} band was randomly perturbed over 5000 iterations based on the band's retrieval error (Fig. 3). The variance of the retrieved Chl-*a* distribution was 1.09 mg m^{-3}. Overall, the performance of MS-MLR on the testing dataset strongly validates the chosen R_{rs} band combination and calculated coefficients. Lastly, Chl_{MLR} performed poorly when used to estimate $a_{\text{CDOM}}(300)$, DOC or SPM. In these cases, the MAE was between 1.19 and 3.07 and MAPE ranged from 65% to 309% (Fig. S3), indicating that these biogeochemical constituents that often interfere with Chl-*a* retrievals in coastal waters have minimum impact on Chl-*a* estimates using this approach.

3.3. OLCI matchup analysis and algorithm evaluation

Evaluation of the MS-MLR algorithm applied to POLYMER-derived OLCI R_{rs} also showed improved performance compared to the other algorithms (Fig. 5, Table 2). The evaluation used a total of 335 valid matchups between OLCI and CTDEEP Chl-*a* data between May 2016 to November 2021. Among the models tested, only MS-MLR and OC4 returned a Chl-*a* value for nearly all matchups ($N_{\text{MLR}} = 322$, $N_{\text{OC4}} = 330$), while the RBD, MDN, and the two-band red-NIR ratio models returned significantly fewer values ($N_{\text{RBD}} = 147$, $N_{\text{MDN}} = 270$, $N_{\text{2-Band}} = 32$). The two-band algorithm failed in so many cases because the base term in the equation (Table S1) was frequently negative. As a result, the two-band algorithm is excluded from further discussion. When comparing the other algorithms, MS-MLR displayed the lowest MAE (0.54) followed by OC4, RBD and MDN (0.7, 0.71 and 0.73 respectively). In addition, MS-MLR showed the lowest bias of 0.22, compared to 0.37 and 0.53 from RBD and OC4, respectively. MDN was the only algorithm that underestimated Chl-*a*, with a bias of −0.25 (Fig. 5, Table 2). Similarly, MS-MLR had the lowest RMSLE and MAPE of all the models. Furthermore, the linear fit between Chl_{MLR} and $\text{Chl}_{\text{insitu}}$ was the closest to the 1:1 line, with a slope approaching 1, capturing the range of Chl-*a* across LIS (Fig. 5, Table 2). MS-MLR had the highest %win (68% vs 57%, 17% and 51% for OC4, RBD and MDN, respectively) (Fig. 5. Table 2). The improved metrics used for this comparison are on par with values used in other studies to choose the best performing algorithm (Pahlevan et al., 2020; Seegers et al., 2018). The relatively poor performance of MDN and RBD is due to the bands used by the algorithms (MDN 400–709 nm and RBD 665–709 nm) which are associated with higher errors and biases (Fig. S2). The use of the 709 nm band by both algorithms also led to the low number of valid retrievals since ~ 25% of the cases this band was negative. OC4 performed poorly, overestimating Chl-*a* at low concentrations, consistent with previous studies (Freitas and Dierssen, 2019). In comparison, MS-MLR relies on spectral bands that are retrieved with relatively low error and bias (Fig. S2) and range from blue to red wavelengths.

To validate that MS-MLR performs as well both spatially and temporally, we evaluated the performance of each algorithm on subsets of the matchup dataset parsed by region (West, Central and East Basins) and season (winter and summer) (Table 2). MS-MLR was the best performing algorithm across most metrics assessed, with the highest %win across all spatial and seasonal subsets. For certain metrics where MS-MLR was not the best performing algorithm, it was MDN that performed better (e.g., MAE in CLIS was 0.65 for MLR vs 0.63 for MDN). Still, even in such cases, MS-MLR returned more valid Chl-*a* values and still had the highest %win. Overall, the MS-MLR algorithm reproduced *in situ* Chl-*a* values with minimal data loss or measurement error. More importantly, MS-MLR was the least biased algorithm and resolved Chl-*a* accurately across the observed range of Chl-*a* in LIS.

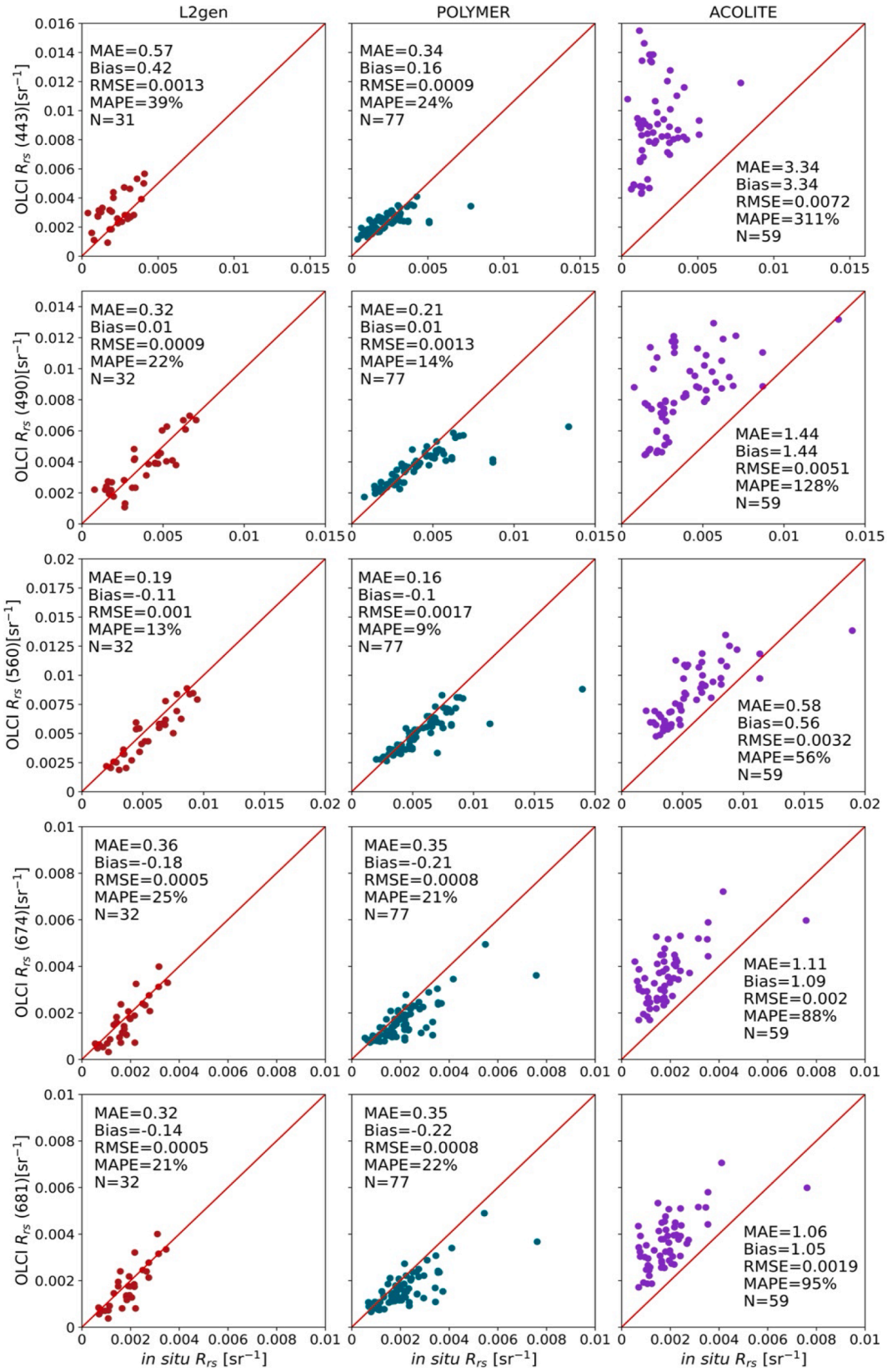

Fig. 3. *In situ* and OLCI R_{rs} derived using L2gen (left), POLYMER (middle) and ACOLITE (right). Red line denotes the 1:1 line. Performance metrics are displayed in each panel.

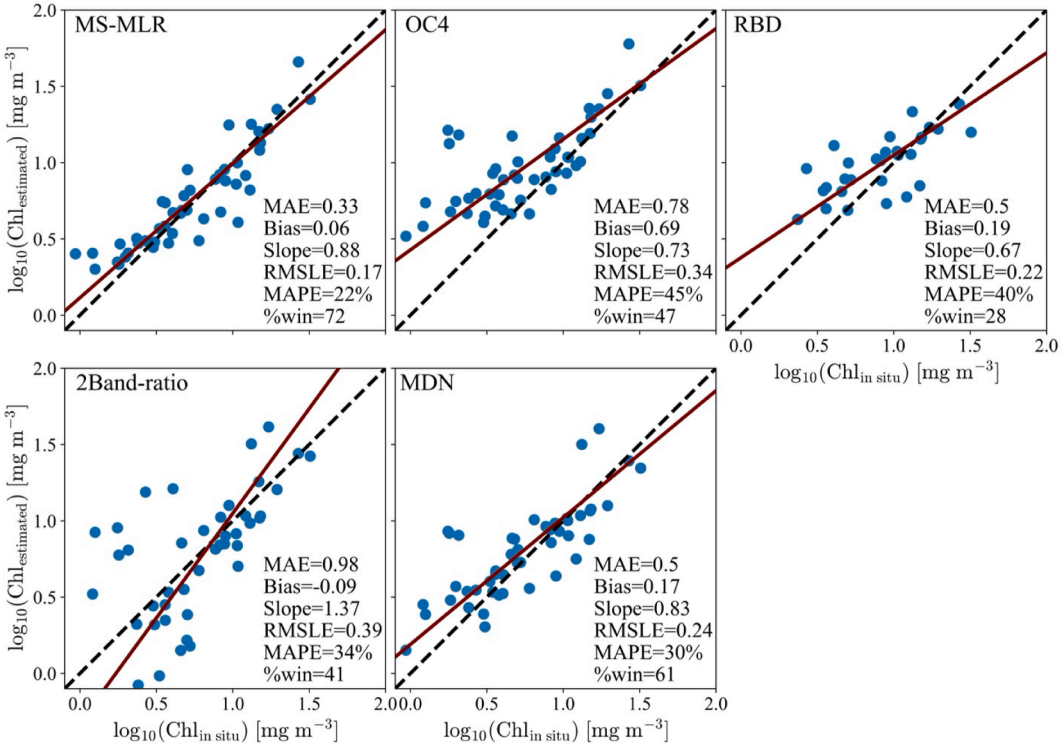

Fig. 4. Performance of Chl-*a* algorithms on testing dataset (1:1 line shown by the black dashed line). The Type-II linear fit is plotted in maroon.

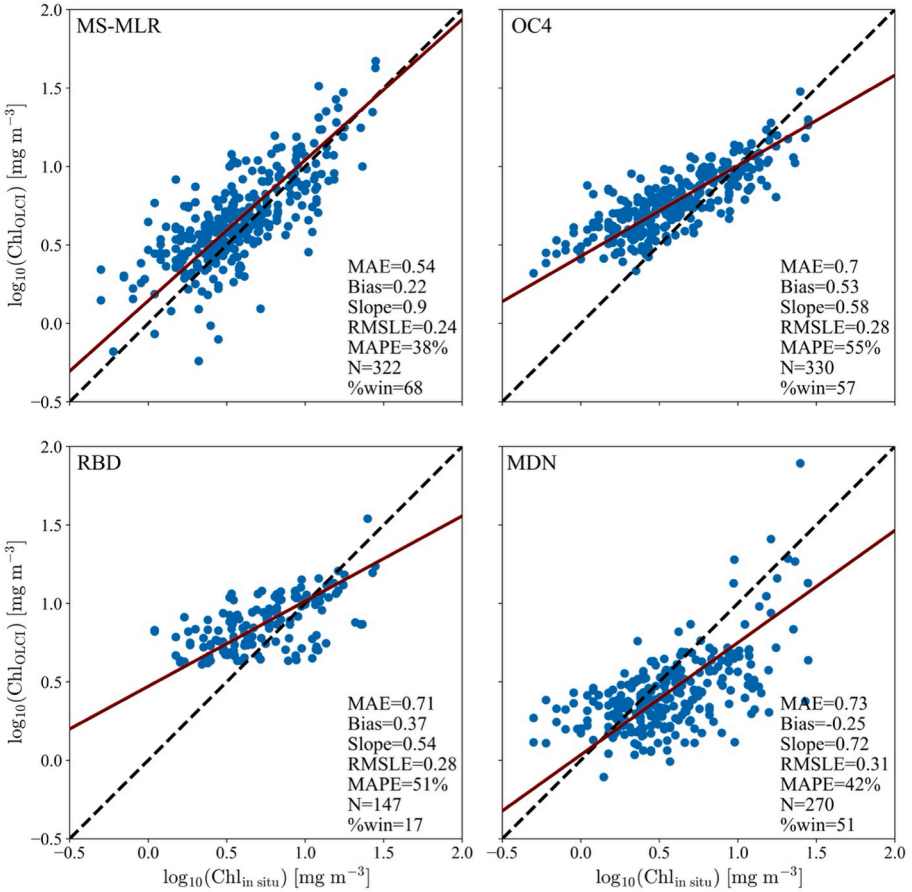

Fig. 5. Performance of Chl-*a* algorithms on matchups between OLCI and CTDEEP Chl-*a* data (N_{valid} = 335) (1:1 line shown by the black dashed line). The Type-II linear fit is plotted in maroon.

Table 2
Performance metrics (MAE, Bias, Slope, RMSLE, MAPE, N and %win), assessed on the full matchup dataset (All) or parsed by region: West, Central and East LIS (WLIS, CLIS, ELIS respectively) and season: Summer (June-Sep) and Winter (Dec-Mar). Bold values indicate the best performing algorithm for each metric.

		All (N = 335)	WLIS (N = 207)	CLIS (N = 70)	ELIS (N = 58)	Summer (N = 155)	Winter (N = 51)
MAE	MS-MLR	**0.54**	**0.48**	0.65	**0.59**	**0.57**	**0.51**
	OC4	0.7	0.57	0.97	0.89	0.6	0.6
	RBD	0.71	0.54	1.3	0.98	0.68	0.79
	MDN	0.73	0.77	**0.63**	0.69	1.08	0.52
Bias	MS-MLR	**0.22**	**0.12**	0.41	0.36	**0.31**	**−0.07**
	OC4	0.53	0.37	0.88	0.75	0.45	0.34
	RBD	0.37	0.15	1.07	0.9	0.54	−0.43
	MDN	−0.25	−0.34	**−0.13**	**−0.02**	−0.47	−0.14
Slope	MS-MLR	**0.9**	**0.98**	**0.78**	**0.83**	0.92	**0.74**
	OC4	0.58	0.59	0.51	0.57	0.6	0.49
	RBD	0.54	0.63	0.51	0.49	0.51	0.38
	MDN	0.72	0.81	0.59	0.56	**0.96**	0.69
RMSLE	MS-MLR	**0.24**	**0.22**	0.27	**0.25**	**0.24**	**0.23**
	OC4	0.28	0.24	0.33	0.35	0.25	0.25
	RBD	0.28	0.23	0.4	0.33	0.28	0.28
	MDN	0.31	0.33	**0.26**	0.28	0.39	**0.23**
MAPE	MS-MLR	**38**	**30**	51	**43**	**41**	38
	OC4	55	44	85	66	43	49
	RBD	51	39	91	118	49	47
	MDN	42	43	**41**	44	50	**36**
N	MS-MLR	322	198	68	56	149	50
	OC4	**330**	**204**	**69**	**57**	**152**	**51**
	RBD	147	100	27	20	84	14
	MDN	270	166	56	48	98	51
%Win	MS-MLR	**68**	**66**	**74**	**64**	**68**	**66**
	OC4	57	58	52	58	64	62
	RBD	17	24	5	8	23	12
	MDN	51	44	60	63	32	59

3.4. Spatial and temporal trends in LIS Chl-a

The superior performance of the MS-MLR approach enables successful integration with long-term water quality monitoring programs toward an improved understanding of spatial gradients and temporal transitions in Chl-*a* across LIS. Consistent with CTDEEP measurements, MS-MLR showed a clear seasonal cycle in Chl-*a* across the Sound with two main blooms, a short-lived early-spring bloom, usually in February-April, followed by a summer or early fall bloom (Fig. 6, upper panel). These seasonal peaks in Chl-*a* showed a decreasing magnitude from west to east (Fig. 6, bottom panels), in agreement with previous studies (Freitas and Dierssen, 2019; Latimer et al., 2014). Satellite imagery during 2016–2021 allowed also to capture interannual variability in the timing, duration, and magnitude of phytoplankton blooms in LIS. In 2018, MS-MLR showed the initiation of the spring bloom in February-March, while an early summer bloom developed in July and a late summer bloom in September (CTDEEP, 2018) (Fig. 6). In 2019, the spring bloom occurred in March and terminated by April, with smaller blooms in May, in agreement with CTDEEP water-quality annual reports (CTDEEP, 2018). The near-daily and high spatial resolution coverage of the entire Sound by OLCI provide observations of fine-scale Chl-*a* dynamics and variability that would otherwise go unobserved with monthly or bi-weekly *in situ* sampling at a limited number of point locations. This accounts for the differences between MS-MLR and CTDEEP observed in Fig. 6 where MS-MLR captures transient events as well as nearshore waters, not sampled by CTDEEP. Binning by region (Fig. 6 bottom panels) further highlights this with higher difference between CTDEEP and MS-MLR in the highly dynamic Western Basin where Chl-*a* often shows patchy blooms and is more impacted by anthropogenic pressures. The shaded regions in Fig. 6 highlight periods when *in situ* sampling was halted due to multiple COVID-19 shutdowns in spring 2020 and winter 2021. Satellite measurements by OLCI, however, uninterruptedly captured phytoplankton dynamics during the COVID-19 pandemic. Interestingly, in April 2020 MS-MLR observed anomalously lower mean Chl-*a* concentrations in the Western LIS compared to the 2017–2019 monthly April mean. This anomaly was observed immediately after the first pandemic wave when strict lockdowns were imposed in NYC. Such measurements are critical for assessing the environmental impacts of the COVID-19 pandemic on LIS ecological functioning.

High-resolution satellite MS-MLR retrievals also reveal spatial dynamics in Chl-*a* beyond what can be inferred by the limited spatial coverage of *in situ* sampling. In addition to the clear west-east spatial gradient, OLCI captured strong transitions in Chl-*a* between the nearshore and open waters of LIS (e.g., high Chl-*a* along the southern shoreline of LIS in February 2020; Fig. 7), as well as in the major river mouths where high nutrient inputs often result in high phytoplankton activity (Fig. 7). MS-MLR also allowed to capture the strong spatial heterogeneity that characterizes Chl-*a* concentrations during the spring and summer algal bloom seasons (Fig. 8). In May 2018 and July 2019, OLCI and CTDEEP measured high Chl-*a* in Western LIS, in excellent

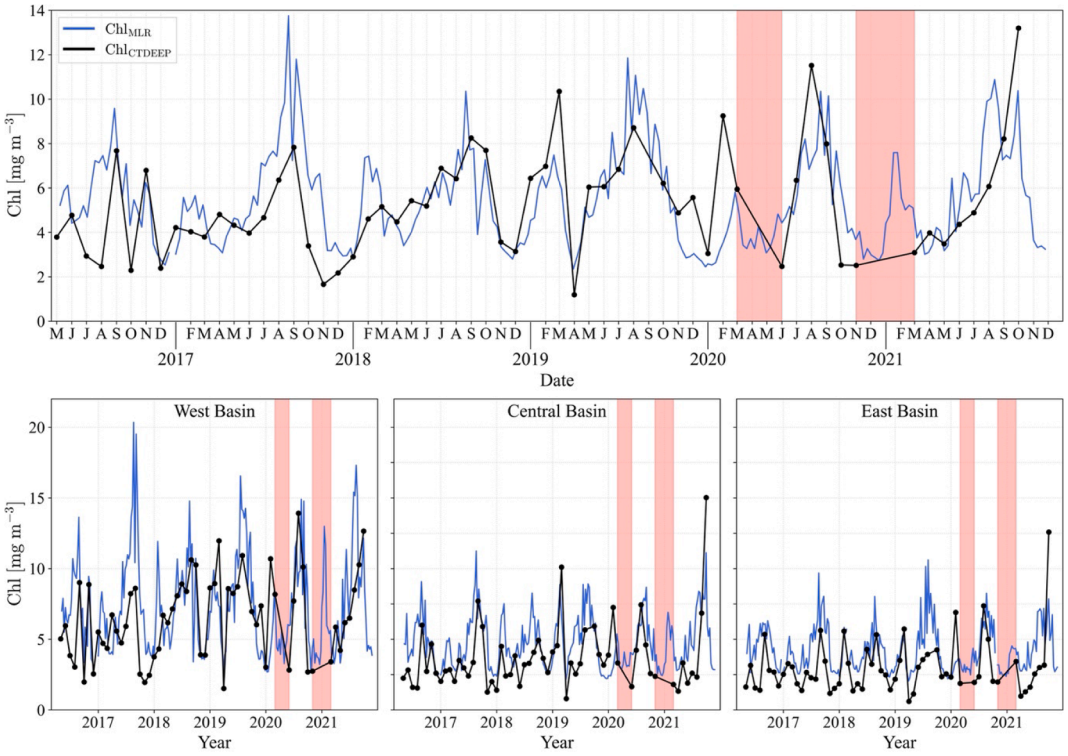

Fig. 6. Chl-*a* time series from CTDEEP (Black) and Chl$_{MLR}$ 8-day averages (blue). Top panel is Chl-*a* averaged over the LIS. Bottom panels are averages by region. Red shaded periods in 2020 and 2021 denote when COVID-19 restrictions halted CTDEEP sampling.

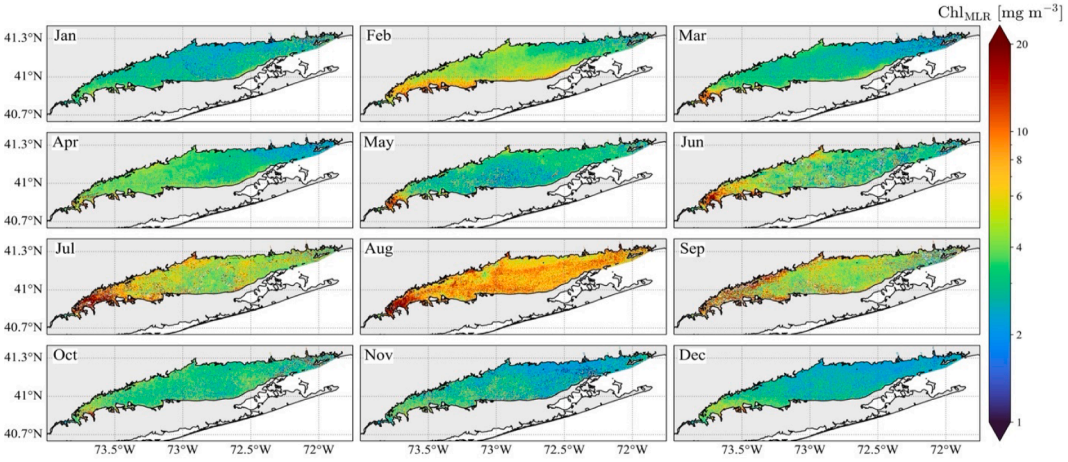

Fig. 7. Monthly composites of Chl$_{MLR}$ retrieved from OLCI during 2020.

agreement (Fig. 8). Yet, MS-MLR uniquely allowed to capture the patchiness and spatial extent of the blooms, which is key for understanding the combined influence of environmental, ecological, and physiological drivers on estuarine Chl-*a* dynamics.

3.5. Application of MS-MLR derived Chl-a for ongoing water quality monitoring in LIS

As part of local, state, and regional efforts to monitor LIS water quality, Save the Sound (STS), a nonprofit organization, has been publishing bi-annual report cards that track and publicize the Sound's ecological health (https://www.savethesound.org/report-card). Based on *in situ* data, these report cards produce water quality grades for major subregions of LIS that can be used by decision makers and environmental protection agencies involved in water quality monitoring, restoration efforts and future infrastructural investments. These water quality grades are based on comparisons of Chl-*a*, dissolved oxygen, water clarity, and DOC concentrations to thresholds and goals defined

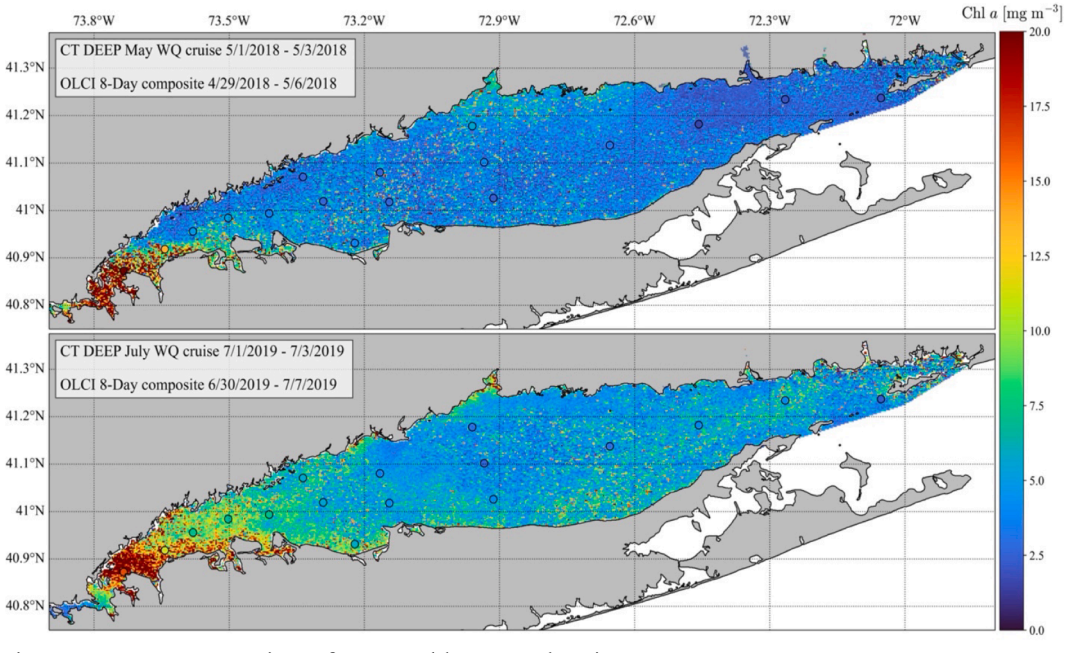

Fig. 8. 8-Day composites of OLCI Chl_{MLR} overlapping *in situ* CTDEEP measurements (circles) in May 2018 (top) and July 2019 (bottom). Color bar reflects both *in situ* and OLCI Chl-*a* values. Textboxes in each panel provide the dates in which CTDEEP sampling occurred, and the OLCI Chl_{MLR} composite date range.

by the U.S. EPA.

With an improved spatiotemporal coverage, satellite observations can provide valuable data products to complement these efforts. Here, we compared the 2019 STS Chl-a grades (from https://soundhealthexplorer.org/fishable/2019/) with the Chl-a grade calculated from Chl_{MLR} following the STS methodology (Fig. 9). When Chl-a values are < 5 mg m^{-3} a grade of 100% is assigned. Conversely a 0% grade is assigned when Chl-a is > 20 mg m^{-3}. Between 5 and 20 mg m^{-3} the grade is calculated from a third-order polynomial, defined as: grade $= -0.1166*Chl^3 + 4.3706*Chl^2 - 54.744*Chl + 279.02$. STS assigns a grade for five open-water regions of LIS (Eastern, Central, and Western Basins, and Eastern and Western Narrows). In the Narrows, water quality is historically the worst due to proximity to the densely populated NYC metropolitan area. As expected, in 2019 STS Chl-a grades followed the spatial trend in Chl-a across the Sound. The high values of Chl-a in the west, primarily in the Narrows, lead to a lower grade compared to the Central and Eastern Basins where Chl-a is low and water quality is better (Fig. 9). Chl-a grades calculated with OLCI closely

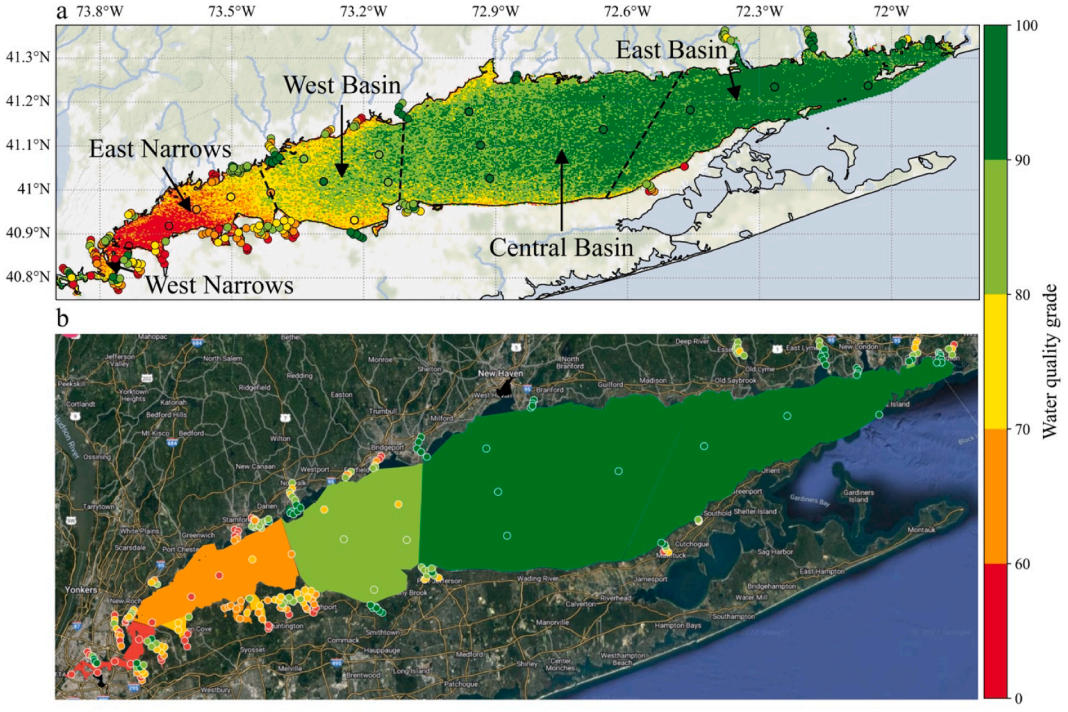

Fig. 9. 2019 Chl-*a* water quality grades calculated with OLCI Chl_{MLR} (a) and Save the Sound grades published in https://soundhealthexplorer.org/fishable/2019/ (b). Circles in both panels are the STS point grades used to grade each region and embayment. Color bar reflects the color scale used by STS.

reflect the STS grades (Fig. 9a). Moreover, OLCI derived grades further highlight the dynamic spatial gradient across the Sound and provide a high-resolution view of the water quality.

4. Conclusions

Applying space-based observations to improve predictive understanding of ecological processes in increasingly vulnerable urban estuaries and coasts requires satellite data products and algorithms optimized to these multifaceted ecosystems where water optical characteristics are highly complex and variable. Previous algorithms have shown the benefit of utilizing the full spectral range available from remote sensing to improve retrievals of water biogeochemical constituents in complex waters (Cao et al., 2018; Cao and Tzortziou, 2021; Pahlevan et al., 2020). Such approaches diverge from other algorithms that rely on a small number of spectral bands, allowing a holistic integration of the spectral data impacted by the underlying water constituents resulting in improved retrievals. To address the need for optimized Chl-*a* algorithms in optically complex waters, we developed an MS-MLR algorithm for OLCI-retrieved R_{rs} that relies on a wide range of spectral bands. The algorithm was validated for LIS, a perfect example of an environment where water quality monitoring efforts are critical for ecological and human health, but in which Chl-*a* remote sensing retrievals are challenging and error prone.

We showed that POLYMER is the preferred AC algorithm for OLCI in LIS, with the lowest error rates and loss of data. MS-MLR performed remarkably well when validated against an *in situ* dataset that represents the full range of seasonal and spatial variability. MS-MLR displayed the lowest MAE and bias in addition to other metrics when compared to other Chl-*a* algorithms. Moreover, it had the highest %win among all models tested, and consistently displayed more accurate Chl-*a* estimates. The improved performance of MS-MLR is due to the use of a wide spectral range, from blue to red, which can better capture the optical complexity of the Sound compared to algorithms that only use the blue-green or red spectral regions. Furthermore, we showed that MS-MLR provides fine-scale spatiotemporal resolution. Lastly, we highlighted the importance of remote sensing observations to monitor water quality when *in situ* measurements cannot be conducted, such as during the COVID-19 related closures.

Increasing demand for and interest in ecosystem protection and restoration necessitates implementation of cost-effective monitoring efforts able to integrate the full scope of available data. The MS-MLR approach described here is such an example that incorporates the wide information embedded in the spectral signature of optically complex waters to derive Chl-*a* with improved accuracy. Employing it across ecosystems and sensors to monitor and study the spatiotemporal dynamics of Chl-*a* requires little computational power to optimize, and provides ecosystem managers, stakeholders, and researchers a synoptic view of ecosystem functioning.

Funding

This research was supported by National Aeronautics and Space Administration (NASA) grants 80NSSC17K0258 (Interdisciplinary Science Program) and 80NSSC20K1287 (Ocean Biology and Biogeochemistry Program), and EPA / NY and CT Sea Grant (NYSG/CTSG) 82913-1156439.

CRediT authorship contribution statement

Jonathan Sherman: Conceptualization, Data curation, Formal analysis, Investigation, Methodology, Software, Validation, Visualization, Writing - original draft, Writing - review & editing. **Maria Tzortziou:** Conceptualization, Methodology, Investigation, Project administration, Supervision, Funding acquisition, Data curation, Formal analysis, Writing - review & editing. **Kyle J. Turner:** Data curation, Investigation, Writing – review & editing. **Joaquim Goes:** Investigation, Data curation, Writing - review & editing. **Brice Grunert:** Data curation, Investigation, Writing - review & editing.

Declaration of Competing Interest

The authors declare that they have no known competing financial interests or personal relationships that could have appeared to influence the work reported in this paper.

Data availability

Data availability statement at end of manuscript

Acknowledgements

The authors would like to thank CTDEEP, including Matt Lyman, Katie O'Brien-Clayton, and Captain Tommy Seda of the *R/V John Dempsey*. We would also like to thank Kali McKee from Lamont–Doherty Earth Observatory for Chl-*a* sample processing. We sincerely thank Nima Pahlevan at NASA Goddard Space Flight Center for his feedback on the MDN algorithm application and this manuscript.

Data Availability

Chl-a data collected from 2017-2021 are available on NASA's SeaBASS archive. *In situ* $R_{rs}(\lambda)$ data, and data collected in 2022 are in preparation for submission to SeaBASS and can be made available upon request.

Appendix A. Supplementary material

Supplementary data to this article can be found online at https://doi.org/10.1016/j.jag.2023.103223.

References

Alvarez-Mendoza, C.I., Teodoro, A.C., Torres, N., Vivanco, V., 2019. Assessment of Remote Sensing Data to Model PM10 Estimation in Cities with a Low Number of Air Quality Stations: A Case of Study in Quito. Ecuador. Environments 6, 85. https://doi.org/10.3390/environments6070085.

Anderson, T.H., Taylor, G.T., 2001. Nutrient Pulses, Plankton Blooms, and Seasonal Hypoxia in Western Long Island Sound, Estuarine Research Federation Estuaries.

Bailey, S.W., Franz, B.A., Werdell, P.J., 2010. Estimation of near-infrared water-leaving reflectance for satellite ocean color data processing. Opt. Express 18, 7521–7527. https://doi.org/10.1364/OE.18.007521.

Bauer, J.E., Cai, W.J., Raymond, P.A., Bianchi, T.S., Hopkinson, C.S., Regnier, P.A.G., 2013. The changing carbon cycle of the coastal ocean. Nature 504, 61–70. https://doi.org/10.1038/nature12857.

Boerema, A., Meire, P., 2017. Management for estuarine ecosystem services: A review. Ecol. Eng. 98, 172–182. https://doi.org/10.1016/j.ecoleng.2016.10.051.

Boyer, J.N., Kelble, C.R., Ortner, P.B., Rudnick, D.T., 2009. Phytoplankton bloom status: Chlorophyll a biomass as an indicator of water quality condition in the southern estuaries of Florida, USA. Ecol. Ind. 9, 56–67. https://doi.org/10.1016/j.ecolind.2008.11.013.

Cao, F., Tzortziou, M., 2021. Capturing dissolved organic carbon dynamics with Landsat-8 and Sentinel-2 in tidally influenced wetland–estuarine systems. Sci. Total Environ. 777, 145910 https://doi.org/10.1016/j.scitotenv.2021.145910.

Cao, F., Tzortziou, M., Hu, C., Mannino, A., Fichot, C.G., Del Vecchio, R., Najjar, R.G., Novak, M., 2018. Remote sensing retrievals of colored dissolved organic matter and dissolved organic carbon dynamics in North American estuaries and their margins. Remote Sens. Environ. 205, 151–165. https://doi.org/10.1016/j.rse.2017.11.014.

CT DEEP, 2018. 2018 Long Island Sound Hypoxia Season Review. Connecticut Department of Energy and Environmental Protection, Bureau of Water Protection and Land Reuse. Hartford, CT 06106.

Freitas, F.H., Dierssen, H.M., 2019. Evaluating the seasonal and decadal performance of red band difference algorithms for chlorophyll in an optically complex estuary with winter and summer blooms. Remote Sens. Environ. 231 https://doi.org/10.1016/j.rse.2019.111228.

Gilerson, A.A., Gitelson, A.A., Zhou, J., Gurlin, D., Moses, W., Ioannou, I., Ahmed, S.A., 2010. Algorithms for remote estimation of chlorophyll-a in coastal and inland waters using red and near infrared bands. Opt. Express 18, 24109. https://doi.org/10.1364/oe.18.024109.

Gitelson, A., 1992. The peak near 700 nm on radiance spectra of algae and water: Relationships of its magnitude and position with chlorophyll. Int. J. Remote Sens. 13, 3367–3373. https://doi.org/10.1080/01431169208904125.

Groetsch, P.M.M., Gege, P., Simis, S.G.H., Eleveld, M.A., Peters, S.W.M., 2017. Validation of a spectral correction procedure for sun and sky reflections in above-water reflectance measurements. Opt. Express 25, A742. https://doi.org/10.1364/oe.25.00a742.

Haraguchi, L., Carstensen, J., Abreu, P.C., Odebrecht, C., 2015. Long-term changes of the phytoplankton community and biomass in the subtropical shallow Patos Lagoon Estuary, Brazil. Estuarine, Coastal Shelf Sci., Special Issue: Global Patterns Phytoplankton Dyn. Coastal Ecosyst. 162, 76–87. https://doi.org/10.1016/j.ecss.2015.03.007.

Holm-Hansen, O., Lorenzen, C.J., Holmes, R.W., Strickland, J.D.H., 1965. Fluorometric determination of chlorophyll. ICES J. Mar. Sci. 30, 3–15. https://doi.org/10.1093/icesjms/30.1.3.

Hu, C., Mullerkarger, F., Taylor, C., Carder, K., Kelble, C., Johns, E., Heil, C., 2005. Red tide detection and tracing using MODIS fluorescence data: A regional example in SW Florida coastal waters. Remote Sens. Environ. 97, 311–321. https://doi.org/10.1016/j.rse.2005.05.013.

Hu, C., Lee, Z., Franz, B., 2012. Chlorophyll a algorithms for oligotrophic oceans: A novel approach based on three-band reflectance difference. J. Geophys. Res. Oceans 117, 1–25. https://doi.org/10.1029/2011JC007395.

Kocian, M., Fletcher, A., Schundler, G., Batker, D., Schwartz, A., Briceno, T., 2015. The trillion dollar asset: The economic value of the Long Island Sound basin. Earth Economics, Tacoma, WA.

Latimer, J.S., Tedesco, M.A., Swanson, R.L., Yarish, C., Stacey, P.E., Garza, C., 2014. Long Island sound: prospects for the urban sea. Springer.

Le, C., Hu, C., English, D., Cannizzaro, J., Chen, Z., Feng, L., Boler, R., Kovach, C., 2013. Towards a long-term chlorophyll-a data record in a turbid estuary using MODIS observations. Prog. Oceanogr. 109, 90–103. https://doi.org/10.1016/j.pocean.2012.10.002.

Livingston, R.J., 2007. Phytoplankton Bloom Effects on a Gulf Estuary: Water Quality Changes and Biological Response. Ecol. Appl. 17, S110–S128. https://doi.org/10.1890/05-0769.1.

Mannino, A., Novak, M.G., Hooker, S.B., Hyde, K., Aurin, D., 2014. Algorithm development and validation of CDOM properties for estuarine and continental shelf waters along the northeastern U.S. coast. Remote Sens. Environ. 152, 576–602. https://doi.org/10.1016/j.rse.2014.06.027.

Maritorena, S., Siegel, D.A., Peterson, A.R., 2002. Optimization of a semianalytical ocean color model for global-scale applications. Appl. Opt. AO 41, 2705–2714. https://doi.org/10.1364/AO.41.002705.

McKinna, L.I.W., Cetinić, I., Werdell, P.J., 2021. Development and Validation of an Empirical Ocean Color Algorithm with Uncertainties: A Case Study with the Particulate Backscattering Coefficient. J. Geophys. Res. Oceans 126. https://doi.org/10.1029/2021JC017231.

McKinna, L.I.W., Cetinić, I., Chase, A.P., Werdell, P.J., 2019. Approach for Propagating Radiometric Data Uncertainties Through NASA Ocean Color Algorithms. Frontiers in Earth Science 7.

Mélin, F., Zibordi, G., Berthon, J.-F., Bailey, S., Franz, B., Voss, K., Flora, S., Grant, M., 2011. Assessment of MERIS reflectance data as processed with SeaDAS over the European seas. Opt. Express 19, 25657. https://doi.org/10.1364/oe.19.025657.

Mobley, C.D., 1999. Estimation of the remote-sensing reflectance from above-surface measurements. Appl. Opt. AO 38, 7442–7455. https://doi.org/10.1364/AO.38.007442.

Mograne, M., Jamet, C., Loisel, H., Vantrepotte, V., Mériaux, X., Cauvin, A., 2019. Evaluation of Five Atmospheric Correction Algorithms over French Optically-Complex Waters for the Sentinel-3A OLCI Ocean Color Sensor. Remote Sens. (Basel) 11, 668. https://doi.org/10.3390/rs11060668.

Moses, W.J., Gitelson, A.A., Berdnikov, S., Saprygin, V., Povazhnyi, V., 2012. Operational MERIS-based NIR-red algorithms for estimating chlorophyll-a concentrations in coastal waters — The Azov Sea case study. Remote Sens. Environ. 121, 118–124. https://doi.org/10.1016/j.rse.2012.01.024.

O'Reilly, J.E., Maritorena, S., Mitchell, B.G., Siegel, D.A., Carder, K.L., Garver, S.A., Kahru, M., McClain, C., 1998. Ocean color chlorophyll algorithms for SeaWiFS. J. Geophys. Res. Oceans 103, 24937–24953. https://doi.org/10.1029/98JC02160.

O'Reilly, J.E., Werdell, P.J., 2019. Chlorophyll algorithms for ocean color sensors - OC4, OC5 & OC6. Remote Sens. Environ. 229, 32–47. https://doi.org/10.1016/j.rse.2019.04.021.

Pahlevan, N., Smith, B., Schalles, J., Binding, C., Cao, Z., Ma, R., Alikas, K., Kangro, K., Gurlin, D., Hà, N., Matsushita, B., Moses, W., Greb, S., Lehmann, M.K., Ondrusek, M., Oppelt, N., Stumpf, R., 2020. Seamless retrievals of chlorophyll-a from Sentinel-2 (MSI) and Sentinel-3 (OLCI) in inland and coastal waters: A machine-learning approach. Remote Sens. Environ. 240 https://doi.org/10.1016/j.rse.2019.111604.

Pahlevan, N., Smith, B., Alikas, K., Anstee, J., Barbosa, C., Binding, C., Bresciani, M., Cremella, B., Giardino, C., Gurlin, D., Fernandez, V., Jamet, C., Kangro, K., Lehmann, M.K., Loisel, H., Matsushita, B., Hà, N., Olmanson, L., Potvin, G., Simis, S. G.H., VanderWoude, A., Vantrepotte, V., Ruiz-Verdù, A., 2022. Simultaneous retrieval of selected optical water quality indicators from Landsat-8, Sentinel-2, and Sentinel-3. Remote Sens. Environ. 270, 112860 https://doi.org/10.1016/j.rse.2021.112860.

Pitarch, J., Talone, M., Zibordi, G., Groetsch, P., 2020. Determination of the remote-sensing reflectance from above-water measurements with the "3C model": a further assessment. Opt. Express, OE 28, 15885–15906. https://doi.org/10.1364/OE.388683.

Seegers, B.N., Stumpf, R.P., Schaeffer, B.A., Loftin, K.A., Werdell, P.J., 2018. Performance metrics for the assessment of satellite data products: an ocean color case study. Opt. Express 26, 7404. https://doi.org/10.1364/oe.26.007404.

Staehr, P.A., Testa, J., Carstensen, J., 2017. Decadal Changes in Water Quality and Net Productivity of a Shallow Danish Estuary Following Significant Nutrient Reductions. Estuar. Coasts 40, 63–79. https://doi.org/10.1007/s12237-016-0117-x.

Steinmetz, F., Deschamps, P.-Y., Ramon, D., 2011. Atmospheric correction in presence of sun glint: application to MERIS. Opt. Express 19, 9783. https://doi.org/10.1364/oe.19.009783.

Trujillo-Ortiz, A., Hernandez-Walls, R., 2010. gmregress: Geometric Mean Regression (Reduced Major Axis Regression). A MATLAB file.

Turner, K.J., Tzortziou, M., Grunert, B.K., Goes, J., Sherman, J., 2022. Optical classification of an urbanized estuary using hyperspectral remote sensing reflectance. Opt. Express 30, 41590. https://doi.org/10.1364/OE.472765.

Tzortziou, M., Parker, O., Lamb, B., Herman, J.R., Lamsal, L., Stauffer, R., Abuhassan, N., 2018. Atmospheric Trace Gas (NO2 and O3) Variability in South Korean Coastal Waters, and Implications for Remote Sensing of Coastal Ocean Color Dynamics. Remote Sens. (Basel) 10, 1587. https://doi.org/10.3390/rs10101587.

Vandermeulen, R.A., Mannino, A., Craig, S.E., Werdell, P.J., 2020. 150 shades of green: Using the full spectrum of remote sensing reflectance to elucidate color shifts in the ocean. Remote Sens. Environ. 247, 111900 https://doi.org/10.1016/j.rse.2020.111900.

Vanhellemont, Q., Ruddick, K., 2021. Atmospheric correction of Sentinel-3/OLCI data for mapping of suspended particulate matter and chlorophyll-a concentration in Belgian turbid coastal waters. Remote Sens. Environ. 256, 112284 https://doi.org/10.1016/j.rse.2021.112284.

Welsh, B.L., Eller, F.C., 1991. Mechanisms controlling summertime oxygen depletion in western Long Island Sound. Estuaries 14, 265–278. https://doi.org/10.2307/1351661.

Werdell, P.J., Franz, B.A., Bailey, S.W., Feldman, G.C., Boss, E., Brando, V.E., Dowell, M., Hirata, T., Lavender, S.J., Lee, Z., Loisel, H., Maritorena, S., Mélin, F., Moore, T.S., Smyth, T.J., Antoine, D., Devred, E., d'Andon, O.H.F., Mangin, A., 2013. Generalized ocean color inversion model for retrieving marine inherent optical properties. Appl. Opt. AO 52, 2019–2037. https://doi.org/10.1364/AO.52.002019.

Werdell, P.J., McKinna, L.I.W., Boss, E., Ackleson, S.G., Craig, S.E., Gregg, W.W., Lee, Z., Maritorena, S., Roesler, C.S., Rousseaux, C.S., Stramski, D., Sullivan, J.M., Twardowski, M.S., Tzortziou, M., Zhang, X., 2018. An overview of approaches and challenges for retrieving marine inherent optical properties from ocean color remote sensing. Prog. Oceanogr. 160, 186–212. https://doi.org/10.1016/j.pocean.2018.01.001.

Whitney, M.M., Vlahos, P., 2021. Reducing Hypoxia in an Urban Estuary despite Climate Warming. Environ. Sci. Tech. 55, 941–951. https://doi.org/10.1021/acs.est.0c03964.

Zibordi, G., Voss, K.J., Johnson, B.C., Mueller, J.L., 2019. IOCCG Ocean Optics and Biogeochemistry Protocols for Satellite Ocean Colour Sensor Validation. IOCCG Protocol Series 3. https://doi.org/10.25607/OBP-691.